

An Observed Evidence for the Primordial Origin of Galaxy Sizes

Jun-Sung Moon^{1,2,3} and Jounghun Lee¹

¹*Department of Physics and Astronomy, Seoul National University, Seoul 08826, Republic of Korea*

²*Research Institute of Basic Sciences, Seoul National University, Seoul 08826, Republic of Korea*

³*Institute of Astronomy and Astrophysics, Academia Sinica, 11F of Astronomy-Mathematics Building, No. 1, Sec. 4, Roosevelt Rd., Taipei 106319, Taiwan, R.O.C.*

ABSTRACT

We present an observational evidence supporting the scenario that the protogalactic angular momenta play the most decisive role in molding the optical sizes of present galaxies. Analyzing the NASA-Sloan Atlas catalog in the redshift range of $0.02 \leq z < 0.09$, we observationally determine the probability density distributions, $p(r_{50})$ and $p(r_{90})$, where r_{50} and r_{90} denote the galaxy sizes enclosing 50% and 90% of their r -band luminosities, respectively. Both of the distributions are found to be well described by a bimodal Gamma mixture model, which is consistent with the recent numerical results. Classifying the local galaxies by their ratios, r_{50}/r_{90} , we also show that for the case of late-type galaxies with $r_{50}/r_{90} \geq 0.45$ both of $p(r_{50})$ and $p(r_{90})$ exhibit no bimodal feature, following a unimodal Gamma model. Assuming the existence of a linear causal correlation between $\{r_{50}, r_{90}\}$ of the late-type galaxies and the primordial spin factor, τ , defined as the degree of misalignments between the initial tidal and protogalaxy inertia tensors, we reconstruct the probability density distributions, $p(\tau)$, directly from the observationally determined $p(r_{50})$ and $p(r_{90})$ of the late-type galaxies, and show excellent agreements with the real distributions of τ which were determined at the protogalactic stages by numerical experiments. A critical implication of our result on reconstructing the initial conditions from observable galaxy sizes is discussed.

Subject headings: Unified Astronomy Thesaurus concepts: Cosmology (343); Large-scale structure of the universe (902)

1. Introduction

The galaxy angular momentum is one of the most fundamental properties that the galaxies possess, the origin of which is believed to be the protogalactic tidal interactions with the surrounding matter distribution (Doroshkevich 1970; White 1984). Until the primordial protogalactic sites decouple from the surrounding matter distribution at the turn-around moments, they steadily acquire angular momenta under the tidal influences, developing causal correlations with the initial tidal fields on the scale of their total masses (Catelan & Theuns 1996; Lee & Pen 2000, 2001). If the angular momenta were perfectly conserved after turning around, then the present galaxies would exhibit strong correlations with the initial conditions. In reality, the galaxy angular momenta are prone to severe modifications during the subsequent nonlinear evolutions, losing much of their memory of the protogalactic states (e.g., Porciani et al. 2002a,b; Vitvitska et al. 2002). Especially, several numerical experiments based on hydrodynamical simulations reported their failures in finding any significant correlations between stellar and dark matter angular momenta of galactic halos (e.g., Jiang et al. 2019, and references therein). Absence of correlations between them were ascribed to the vulnerability of baryonic components to complicated non-gravitational astrophysical processes associated with gas inflow and star formation, which implied no existence of any connections between observable stellar angular momenta of present galaxies and initial tidal fields.

Nonetheless, recent numerical and observational studies have revealed that the stellar angular momenta of present galaxies still retain non-negligible correlations with the initial conditions. For instance, Motloch et al. (2021) detected a $\sim 2.7\sigma$ signal of correlations between spin directions of local spiral galaxies extracted from the Galaxy Zoo data (Land et al. 2008; Lintott et al. 2008) and principal axes of the linear tidal fields reconstructed by the ELUCID collaborations (Wang et al. 2016, 2014). Cadiou et al. (2022) performed multiple zoom-in hydrodynamical simulations and showed that the protogalactic angular momenta have causal effects on the magnitudes of stellar angular momenta of present galactic halos by controlling their merging processes. Moon & Lee (2023) found by analyzing the galactic halos identified in a high-resolution cosmological hydrodynamical simulation that their stellar angular momenta exhibit significantly strong alignments with the principal axes of the initial tidal fields and that the alignment strengths depend on the degree of misalignments between initial tidal and protogalactic inertia tensors. These numerical and observational evidences support the theoretical claim that the galaxy angular momenta can in principle be used to reconstruct the initial tidal and density fields (Lee & Pen 2000, 2001) and to constrain the early universe physics like large-scale parity violation, neutrino masses, and dark energy equation of state (Yu et al. 2019, 2020; Lee et al. 2020; Lee & Libeskind 2020; Shim et al. 2024).

Two different approaches have been taken in the previous studies to investigate the connections between galaxy angular momenta and initial conditions. In one approach the directions of galaxy angular momenta and their alignments with the principal axes of initial tidal fields are the primary subjects. Meanwhile the other approach concerns the galaxy spin parameters (Bullock et al. 2001) and their dependence on the magnitudes of protogalaxy angular momenta. The two approaches have their own merits and drawbacks, complementing each other and providing independent information on the effects of initial conditions on galaxy angular momenta.

The best merit of the first approach is its observational feasibility. Under the key assumption that the observable angular momenta of galaxy stellar components are well aligned with those of dark matter counterparts, the spin axes of spiral galaxies can be determined with two-fold degeneracy from information on their position and inclination angles as well as their axial ratios (e.g. Lee 2011). Recent numerical works, however, casted a doubt on this key assumption by showing that the stellar angular momenta of spiral galaxies exhibit not only misalignments with those of DM counterparts but also quite a different tendency of alignments with the principal axes of initial tidal fields (Moon & Lee 2023). Besides, this approach requires a valid reconstruction of the initial tidal field on the galactic scale $< 0.5h^{-1}\text{Mpc}$, which is difficult to achieve in practice (Motloch et al. 2021).

The second approach based on the magnitudes of galaxy angular momenta has been regarded as being less attainable due to the practical difficulty in determining the galaxy spin parameters from real observations. A clue about how to overcome this difficulty, however, has recently been found in the work of Moon & Lee (2025), according to which the observable galaxy stellar sizes share significant amount of mutual information with the primordial spin factors that are directly proportional to the magnitudes of protogalactic angular momenta. Their results implied that instead of the galaxy spin parameters the observable galaxy sizes can be used to investigate how much memory the angular momenta of present galaxies have for the magnitudes of protogalaxy angular momenta. In this Letter, we attempt to observationally prove that the primordial spin factors have indeed causal effects on the galaxy optical sizes by reconstructing the probability density distributions of the former from those of the observable latter.

2. Observational Determination of the Galaxy Size Distributions

Our analysis utilizes the NASA-Sloan Atlas catalog that compiles the photometric images and shape parameters of local galaxies (Blanton et al. 2011) observed by the Sloan Digital Sky Survey (Alam et al. 2015; Albareti et al. 2017) and Galaxy Evolution Ex-

plorer (Bianchi & GALEX Team 1999). The catalog includes information on the galaxy half-light and 90%-light sizes (r_{50} and r_{90} , respectively) determined in the r -band via the most reliable *elliptical Petrosian aperture photometry* (Wake et al. 2017). For a proper determination of the probability distributions, $p(r_{50})$ and $p(r_{90})$, of the NASA-Sloan Atlas galaxies, it is necessary to exclude those galaxies with angular sizes smaller than the photometric seeing (FWHM) since their values of r_{50} and r_{90} are likely to be overestimated (Shen et al. 2003; Masters et al. 2010).

Given that the angular sizes of local galaxies vary not only with redshifts but also with stellar masses, M_* , we split the ranges of $m_* \equiv \log [M_*/(h^{-1}M_\odot)]$ into three intervals: $[9.5, 10)$, $[10, 10.5)$ and $[10.5, 11]$ and find the galaxies belonging into each m_* -bin at redshifts $z \geq z_{\min} = 0.02$, using information provided by the NASA-Sloan Atlas catalog information on M_* . We set a minimum redshift z_{\min} because large galaxies at low redshifts can be excluded from the spectroscopic sample due to their very bright apparent magnitudes. Then, in each m_* -interval, we take the following three steps to determine the maximum redshift, z_{\max} , beyond which the galaxy angular sizes drop below the photometric seeing.

- Among the galaxies belonging to the upper 95% in the values of r_{50} at z_{\min} , find its lowest value, $r_{50,\min}$, which serves as the lower limit of r_{50} for galaxies within the mass bin.
- Determine the maximum redshift, z_{\max} , at which $r_{50,\min}$ matches the SDSS median photometric seeing (1.32 arcsec in r -band).
- Select only those galaxies which satisfy two conditions of $r_{50} \geq r_{50,\min}$ and $z_{\min} \leq z \leq z_{\max}$.

Figure 1 shows the redshift cutoff values (red vertical lines) determined via the above procedure in each m_* -interval. Through this procedure, we create three size-limited samples containing only those NASA-Sloan Atlas galaxies located at redshifts lower than z_{\max} to obtain reliable size distributions. A total of 13370, 26783 and 58514 galaxies are found to be included in the three controlled samples corresponding to the three m_* -ranges in an increasing order.

For each sample, we split the range of r_{50} into multiple bins of equal length, Δr_{50} , and count the number, ΔN , of those galaxies whose half-light sizes fall in each r_{50} -bin. The probability density, $p(r_{50})$, at each r_{50} -bin is computed as $p(r_{50}) = \Delta N / (N \Delta r_{50})$. Figure 2 plots $p(r_{50})$ (filled red circles) with Poisson errors from each of the three samples in the top panels, clearly demonstrating its bimodal feature in all of the three m_* -ranges. This

observational result is consistent with the recent numerical finding that the probability density distributions of stellar sizes are very well described by the following Gamma mixture model (Moon & Lee 2025):

$$p(r) = \xi p(r; k_1, \theta_1) + (1 - \xi) p(r; k_2, \theta_2) . \quad (1)$$

Here, $p(r; k, \theta)$ is the Gamma distribution defined as

$$p(r; k, \theta) = \frac{1}{\Gamma(k)\theta^k} r^{k-1} \exp\left(-\frac{r}{\theta}\right) , \quad (2)$$

with Gamma function $\Gamma(k)$ and two adjustable parameters $\{k, \theta\}$. Note that the bimodal Gamma mixture model given in Equation (1) is characterized by five adjustable parameters, $\{k_i, \theta_i\}_{i=1}^2$ and ξ , where ξ denotes the fraction of two Gamma modes.

Fitting Equation (1) to the observationally obtained $p(r_{50})$, we determine the best-fit values of $\{k_i, \theta_i\}_{i=1}^2$ and ξ with the help of the χ^2 -statistics. Figure 2 shows the best-fit Gamma mixture model for $p(r_{50})$ (black thick lines), revealing good agreements between the analytic models and numerical results in all of the three m_\star -ranges. Note that the bimodal feature of $p(r_{50})$ becomes less conspicuous in a higher m_\star -range. Given that the galaxies with higher m_\star tend to consist of early-type galaxies, this result implies a possible correlation between galaxy morphology and the bimodality of galaxy size distributions.

To explore this implication further, we classify the galaxies in each m_\star -range into two subsamples according to the ratios, r_{50}/r_{90} , a measure of their concentrations that are known to reflect quite well their morphologies (Oh et al. 2013, and references therein). The threshold of this ratio is set at the conservative value of 0.45 (Park & Choi 2005), which is often adopted to segregate late-type galaxies ($r_{50}/r_{90} \geq 0.45$) from early-type ones ($r_{50}/r_{90} < 0.45$). Then, we separately determine $p(r_{50})$ from each subsample in each m_\star -range and find the best-fit parameters of the Gaussian mixture model with the help of the χ^2 -statistics, the results of which are shown in the middle and bottom panels of Figure 2.

As can be seen, the early-type galaxies with $r_{50}/r_{90} < 0.45$ exhibit highly bimodal distributions (middle panels), yielding the best-fit value of $\xi \sim 0.5$ in each m_\star -range. Whereas, for the case of late-type galaxies (bottom panels), the size distributions show no bimodal feature ($\xi = 0$), being well described by the *unimodal* Gamma distribution (Eq. [2]) alone in all of the three m_\star -ranges. We repeat the whole process but with the 90%-light sizes and show the results in Figure 3. As can be seen the behaviors and trends of $p(r_{90})$ are very similar to those of $p(r_{50})$. Especially, the degree of bimodality of $p(r_{90})$ is also strongly dependent on the ratio, r_{50}/r_{90} , becoming negligibly low for the late-type case just like that of $p(r_{50})$. These results imply that the galaxy optical size distributions must develop their bimodal features during the relaxation processes after their latest major merger events.

Given the previous numerical findings that the spin parameters of galactic halos are found to have the strongest causal correlations with protogalactic angular momenta (Moon & Lee 2024a) and to follow the unimodal Gamma distribution (Moon & Lee 2024b), another critical implication of the results shown in the bottom panels of Figures 2–3 is that for the investigation of correlations between galaxy optical sizes and protogalactic angular momenta, the best target should be the late-type galaxies with $r_{50}/r_{90} > 0.45$. If the protogalactic angular momenta are indeed causally correlated with the galaxy optical sizes, then the probability density distributions of two quantities could be converted to each other. In other words, if the probability density distributions converted from the observed galaxy optical size distributions turn out to reproduce the behaviors and shapes of real protogalactic angular momenta distributions determined in the numerical experiments, it will observationally support the existence of such causal correlations.

Hereafter, we will focus only on the late-type galaxies and use their optical size distributions to reconstruct the distributions of protogalactic angular momenta. Table 1 provides information on the number of late-type galaxies (second column) the best-fit parameters of the unimodal Gamma model (third and fourth columns), and the minimum physical sizes (seventh column) in the three m_* -ranges. The values inside the parentheses correspond to the 90%-light sizes.

3. Reconstruction of the Primordial Spin Factor Distributions

According to the linear tidal torque theory (Doroshkevich 1970; White 1984; Catelan & Theuns 1996; Lee & Pen 2000), the protogalactic angular momenta are directly proportional to the degree of misalignments between the principal axes of two tensors, (I_{ij}) and (T_{ij}) (protogalactic inertia and initial tidal tensors, respectively), which Moon & Lee (2024a) quantified as

$$\tau \equiv \left(\frac{I_{12}^2 + I_{23}^2 + I_{31}^2}{I_{11}^2 + I_{22}^2 + I_{33}^2} \right)^{1/2}, \quad (3)$$

in the principal frame of (T_{ij}) . Moon & Lee (2024b) numerically derived its probability density distribution, $p(\tau)$, and found it to be well approximated by the unimodal Gamma model (Eq. [2]), regardless of the scales used to smooth (T_{ij}) . Noting that $p(\tau)$ tends to have broader shapes on larger scales, they claimed that this scale dependence of $p(\tau)$ represent multi-scale tidal influences on the protogalactic angular momenta.

In the follow-up work of Moon & Lee (2025) based on high-resolution hydrodynamical simulations, it has been revealed that the primordial spin factor, τ , shares significantly large amount of mutual information with the stellar-mass sizes of galactic halos and that their

correlations are almost linear, albeit with large scatters (see Figure 5 in Moon & Lee 2025). Given the result of Moon & Lee (2025), we model τ as

$$\tau = \alpha (r - r_{\min}), \quad \text{for } r \in \{r_{50}, r_{90}\}, \quad (4)$$

where α is the slope of the linear correlation between r and τ . To statistically take into account the scatters in the linear correlations between r and τ , we treat α as a Gaussian random variable with mean $\langle\alpha\rangle$ and standard deviation σ_α .

Equation (4) enables us to reconstruct the probability density distribution of τ from the Gamma distributions that the observed size distributions of the late-type galaxies are found to follow in Section 2:

$$\begin{aligned} p(\tau) &= \int_0^\infty p(r[\tau], \alpha) d\alpha = \int_0^\infty p\left(\frac{\tau}{\alpha} + r_{\min}, \alpha\right) d\alpha \\ &= \frac{1}{\sqrt{2\pi}\sigma_\alpha} \frac{1}{\Gamma(k)\theta^k} \int_0^\infty \left(\frac{\tau}{\alpha} + r_{\min}\right)^{k-1} e^{(-[\tau/\alpha + r_{\min}]/\theta)} \exp\left(-\frac{[\alpha - \langle\alpha\rangle]^2}{2\sigma_\alpha^2}\right) d\alpha, \end{aligned} \quad (5)$$

where $p(r, \alpha) = p(r)p(\alpha)$. Numerically computing the integration in Equation (5), we reconstruct $p(\tau)$ first from $p(r_{50})$, which are shown in Figure 4. For these plots, the two characteristic parameters of the Gamma distribution, $\{k, \theta\}$, are set at the best-fit values (see Table 1) determined in Section 2, while the mean slope and standard deviation of the linear r – τ correlations, $\{\langle\alpha\rangle, \sigma_\alpha\}$, are set at the numerical values determined by Moon & Lee (2025) (given in the fifth column of Table 1). Comparing the reconstructed $p(\tau)$ with the real distributions that Moon & Lee (2024b) determined at $z = 127$ by directly measuring the misalignments between protogalactic inertia and initial tidal tensors (see the top-left panel of Figure 1 in Moon & Lee 2024b), we find that the reconstructed distributions indeed reproduce excellently the shapes, behaviors and *scale*-dependences of the real distributions.

It is worth mentioning here that reconstructing $p(\tau)$ in three different m_\star -ranges is equivalent to reconstructing them on three different smoothing scales, since the protogalactic angular momenta of the galaxies belonging to a different m_\star -range are generated by the initial tidal field smoothed on a different scale. As shown in Moon & Lee (2024b), the shape-variation of $p(\tau)$ is caused by the *differences* between the smoothing scale of the initial tidal field and the Lagrangian radius of protogalactic halos, but not by their individual values. A larger difference between the two scales has an effect of broadening $p(\tau)$ and shifting τ_{\max} to a higher-value where $\tau_{\max} \equiv \operatorname{argmax}_\tau p(\tau)$.

Therefore, the variation of $p(\tau)$ with smoothing scales in a single m_\star -range is expected to be the same as its variation with m_\star on a single smoothing scale. This logic explains why the reconstructed distributions, $p(\tau)$, shown in Figure 4 match the real distributions

obtained on three different scales in a single m_* -range, although we use the values of $\{\langle\alpha\rangle, \sigma_\alpha\}$ determined at three different m_* ranges on a single smoothing scale. We also reconstruct $p(\tau)$ from $p(r_{90})$ via the same procedure and obtain the identical results in each m_* -range. This result implies that both of $p(r_{50})$ and $p(r_{90})$ are equally powerful for the reconstruction of the same $p(\tau)$ when the corresponding values of $\{k, \theta\}$ and $\langle\alpha\rangle$ and σ_α are appropriately plugged in Equation (5).

4. Summary and Discussion

Deriving the probability density distributions of the galaxy half-light and 90%-light sizes, $\{p(r_{50}), p(r_{90})\}$, by analyzing the NASA-Sloan Atlas catalog, we have for the first time discovered that the observationally obtained $\{p(r_{50}), p(r_{90})\}$ follow the bimodal Gamma mixture model, refuting the conventionally accepted log-normal model (e.g., Shen et al. 2003). It has also been found that the degree of bimodality of $\{p(r_{50}), p(r_{90})\}$ depends on the ratio, r_{50}/r_{90} , and that the late-type galaxies with lower concentrations of $r_{50}/r_{90} \geq 0.45$ are best-described by the unimodal Gamma model. Whereas, the early-type galaxies with higher concentrations of $r_{50}/r_{90} < 0.45$ have turned out to possess distinct bimodal features, which implies that the relaxation process after the latest major merging should be responsible for the observed bimodality of galaxy optical size distributions.

In light of the recent numerical result of Moon & Lee (2025), we have assumed the existence of a linear causal correlation between the optical sizes of late-type galaxies and primordial spin factor (τ) defined as the degree of misalignments between protogalactic inertia and initial tidal tensors. In the linear tidal torque theory, the factors, τ , are directly proportional to the magnitudes of protogalactic angular momenta (White 1984; Catelan & Theuns 1996; Lee & Pen 2000). Under this assumption, we have reconstructed the probability density distributions, $p(\tau)$, from the observed $\{p(r_{50}), p(r_{90})\}$ of the late-type galaxies in three different stellar-mass ranges. It has been revealed that the reconstructed $p(\tau)$ reproduces excellently the overall shapes and scale-dependent trends of the real distributions computed at the protogalactic stages in the previous numerical work of Moon & Lee (2024b). This result stands the first observational evidence for the primordial origin of the optical sizes of late-type galaxies.

Although the main focus of the current work has been the reconstruction of $p(\tau)$, our result implies that it should in principle be possible to reconstruct the whole τ -fields, $\tau(\mathbf{x})$, on galactic scales from the observable galaxy optical size fields by employing the iterative reconstruction algorithm as in Lee & Pen (2000, 2001). The algorithm was originally developed for the reconstruction of the initial tidal and density fields from the spin axes. The galaxy

optical sizes have a couple of advantages over the galaxy spin axes for the reconstruction of initial conditions. First, the former is a more readily measurable quantity than the latter, the determination of which is well known to suffer from a degeneracy between the clock-wise and counter clock-wise directions (Lee 2011). Second, unlike the galaxy spin axes that can reconstruct only the rescaled version of initial tidal fields having unity amplitudes (Lee & Pen 2001), the galaxy optical sizes can reconstruct the full version of initial tidal fields since they are connected with the *magnitudes* of protogalactic angular momenta. Our future work is in the direction of reconstructing the initial conditions from the optical sizes of local late-type galaxies and of investigating if and how the reconstructed initial conditions can constrain the early universe physics. We hope to report the result elsewhere in the near future.

Funding for SDSS-III has been provided by the Alfred P. Sloan Foundation, the Participating Institutions, the National Science Foundation, and the U.S. Department of Energy. The SDSS-III web site is <http://www.sdss3.org>. SDSS-III is managed by the Astrophysical Research Consortium for the Participating Institutions of the SDSS-III Collaboration including the University of Arizona, the Brazilian Participation Group, Brookhaven National Laboratory, University of Cambridge, University of Florida, the French Participation Group, the German Participation Group, the Instituto de Astrofísica de Canarias, the Michigan State/Notre Dame/JINA Participation Group, Johns Hopkins University, Lawrence Berkeley National Laboratory, Max Planck Institute for Astrophysics, New Mexico State University, New York University, Ohio State University, Pennsylvania State University, University of Portsmouth, Princeton University, the Spanish Participation Group, University of Tokyo, University of Utah, Vanderbilt University, University of Virginia, University of Washington, and Yale University. The GALEX is a NASA Small Explorer. The mission was developed in cooperation with the Centre National d’Etudes Spatiales of France and the Korean Ministry of Science and Technology.

JSM acknowledges the support by the NRF of Korea grant funded by the Korean government (MEST) (No. 2019R1A6A1A10073437). JL acknowledges the support by Basic Science Research Program through the National Research Foundation (NRF) of Korea funded by the Ministry of Education (RS-2025-00512997).

REFERENCES

- Alam, S., Albareti, F. D., Allende Prieto, C., et al. 2015, *ApJS*, 219, 1, 12. doi:10.1088/0067-0049/219/1/12
- Albareti, F. D., Allende Prieto, C., Almeida, A., et al. 2017, *ApJS*, 233, 2, 25. doi:10.3847/1538-4365/aa8992
- Bianchi, L. & GALEX Team 1999, *Mem. Soc. Astron. Italiana*, 70, 365.
- Blanton, M. R., Kazin, E., Muna, D., et al. 2011, *AJ*, 142, 1, 31. doi:10.1088/0004-6256/142/1/31
- Bullock, J. S., Dekel, A., Kolatt, T. S., et al. 2001, *ApJ*, 555, 1, 240. doi:10.1086/321477
- Catelan, P. & Theuns, T. 1996, *MNRAS*, 282, 436. doi:10.1093/mnras/282.2.436
- Cadiou, C., Pontzen, A., & Peiris, H. V. 2022, *MNRAS*, 517, 3, 3459. doi:10.1093/mnras/stac2858
- Doroshkevich, A. G. 1970, *Astrofizika*, 6, 581.
- Finkbeiner, D. P., Schlafly, E. F., Schlegel, D. J., et al. 2016, *ApJ*, 822, 2, 66. doi:10.3847/0004-637X/822/2/66
- Forero-Romero, J. E., Contreras, S., & Padilla, N. 2014, *MNRAS*, 443, 1090
- Jiang, F., Dekel, A., Kneller, O., et al. 2019, *MNRAS*, 488, 4, 4801. doi:10.1093/mnras/stz1952
- Land, K., Slosar, A., Lintott, C., et al. 2008, *MNRAS*, 388, 4, 1686. doi:10.1111/j.1365-2966.2008.13490.x
- Lee, J. & Pen, U.-L. 2000, *ApJ*, 532, L5.
- Lee, J. & Pen, U.-L. 2001, *ApJ*, 555, 106. doi:10.1086/321472
- Lee, J. 2011, *ApJ*, 732, 2, 99. doi:10.1088/0004-637X/732/2/99
- Lee, J., Libeskind, N. I., & Ryu, S. 2020, *ApJ*, 898, L27
- Lee, J. & Libeskind, N. I. 2020, *ApJ*, 902, 22. doi:10.3847/1538-4357/abb314
- Lee, J. & Moon, J.-S. 2023, *ApJ*, 951, 2, L26. doi:10.3847/2041-8213/acdd75

- Lintott, C. J., Schawinski, K., Slosar, A., et al. 2008, MNRAS, 389, 3, 1179. doi:10.1111/j.1365-2966.2008.13689.x
- Masters, K. L., Nichol, R., Bamford, S., et al. 2010, MNRAS, 404, 2, 792. doi:10.1111/j.1365-2966.2010.16335.x
- Moon, J.-S. & Lee, J. 2023, ApJ, 952, 2, 101. doi:10.3847/1538-4357/acd9ac
- Moon, J.-S. & Lee, J. 2024a, JCAP, 2024, 5, 111. doi:10.1088/1475-7516/2024/05/111
- Moon, J.-S. & Lee, J. 2024b, ApJ, 966, 1, 100. doi:10.3847/1538-4357/ad3825
- Moon, J.-S. & Lee, J. 2025, JCAP, 2025, 3, 018. doi:10.1088/1475-7516/2025/03/018
- Motloch, P., Yu, H.-R., Pen, U.-L., et al. 2021, Nature Astronomy, 5, 283. doi:10.1038/s41550-020-01262-3
- Motloch, P., Pen, U.-L., & Yu, H.-R. 2022, Phys. Rev. D, 105, 8, 083512. doi:10.1103/PhysRevD.105.083512
- Oh, K., Choi, H., Kim, H.-G., et al. 2013, AJ, 146, 6, 151. doi:10.1088/0004-6256/146/6/151
- Park, C. & Choi, Y.-Y. 2005, ApJ, 635, 1, L29. doi:10.1086/499243
- Porciani, C., Dekel, A., & Hoffman, Y. 2002a, MNRAS, 332, 325. doi:10.1046/j.1365-8711.2002.05305.x
- Porciani, C., Dekel, A., & Hoffman, Y. 2002b, MNRAS, 332, 339. doi:10.1046/j.1365-8711.2002.05306.x
- Shen, S., Mo, H. J., White, S. D. M., et al. 2003, MNRAS, 343, 3, 978. doi:10.1046/j.1365-8711.2003.06740.x
- Shim, J., Pen, U.-L., Yu, H.-R., et al. 2024, , arXiv:2406.06080. doi:10.48550/arXiv.2406.06080
- Vitvitska, M., Klypin, A. A., Kravtsov, A. V., et al. 2002, ApJ, 581, 2, 799. doi:10.1086/344361
- Wake, D. A., Bundy, K., Diamond-Stanic, A. M., et al. 2017, AJ, 154, 3, 86. doi:10.3847/1538-3881/aa7ecc
- Wang, H., Mo, H. J., Yang, X., et al. 2016, ApJ, 831, 2, 164. doi:10.3847/0004-637X/831/2/164

- Wang, H., Mo, H. J., Yang, X., et al. 2014, *ApJ*, 794, 1, 94. doi:10.1088/0004-637X/794/1/94
- Wechsler, R. H., Bullock, J. S., Primack, J. R., et al. 2002, *ApJ*, 568, 1, 52. doi:10.1086/338765
- White, S. D. M. 1984, *ApJ*, 286, 38. doi:10.1086/162573
- Yu, H.-R., Pen, U.-L., & Wang, X. 2019, *Phys. Rev. D*, 99, 12, 123532. doi:10.1103/PhysRevD.99.123532
- Yu, H.-R., Motloch, P., Pen, U.-L., et al. 2020, *Phys. Rev. Lett.*, 124, 10, 101302. doi:10.1103/PhysRevLett.124.101302

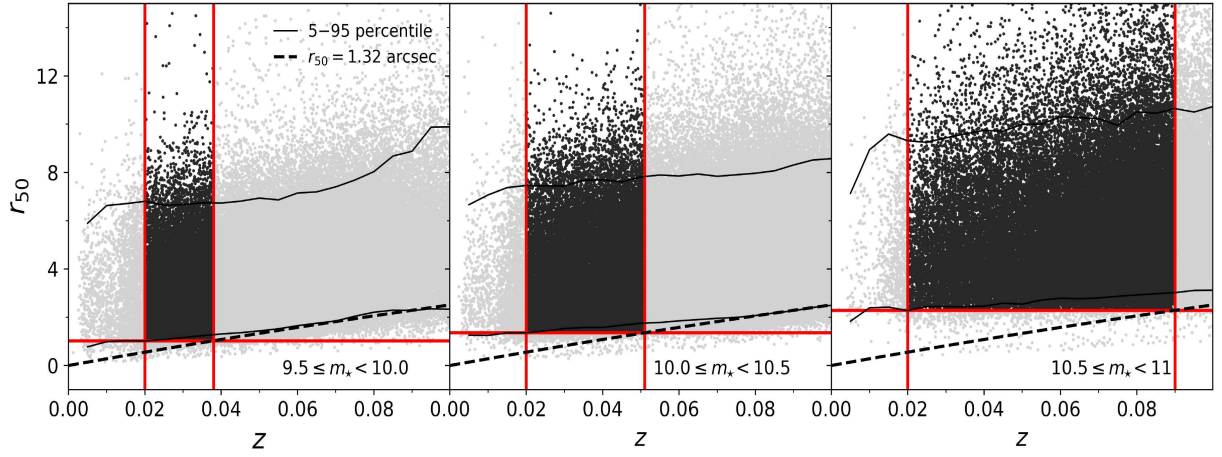


Fig. 1.— Scatter plots of the redshifts and the half-light sizes of the NASA-Sloan-Atlas galaxies in three different stellar-mass ranges, with the locations of two redshift cutoffs, z_{\min} and z_{\max} (vertical red lines) applied to exclude those galaxies the angular sizes of which are smaller than the photometry seeing at z_{\max} (horizontal red lines).

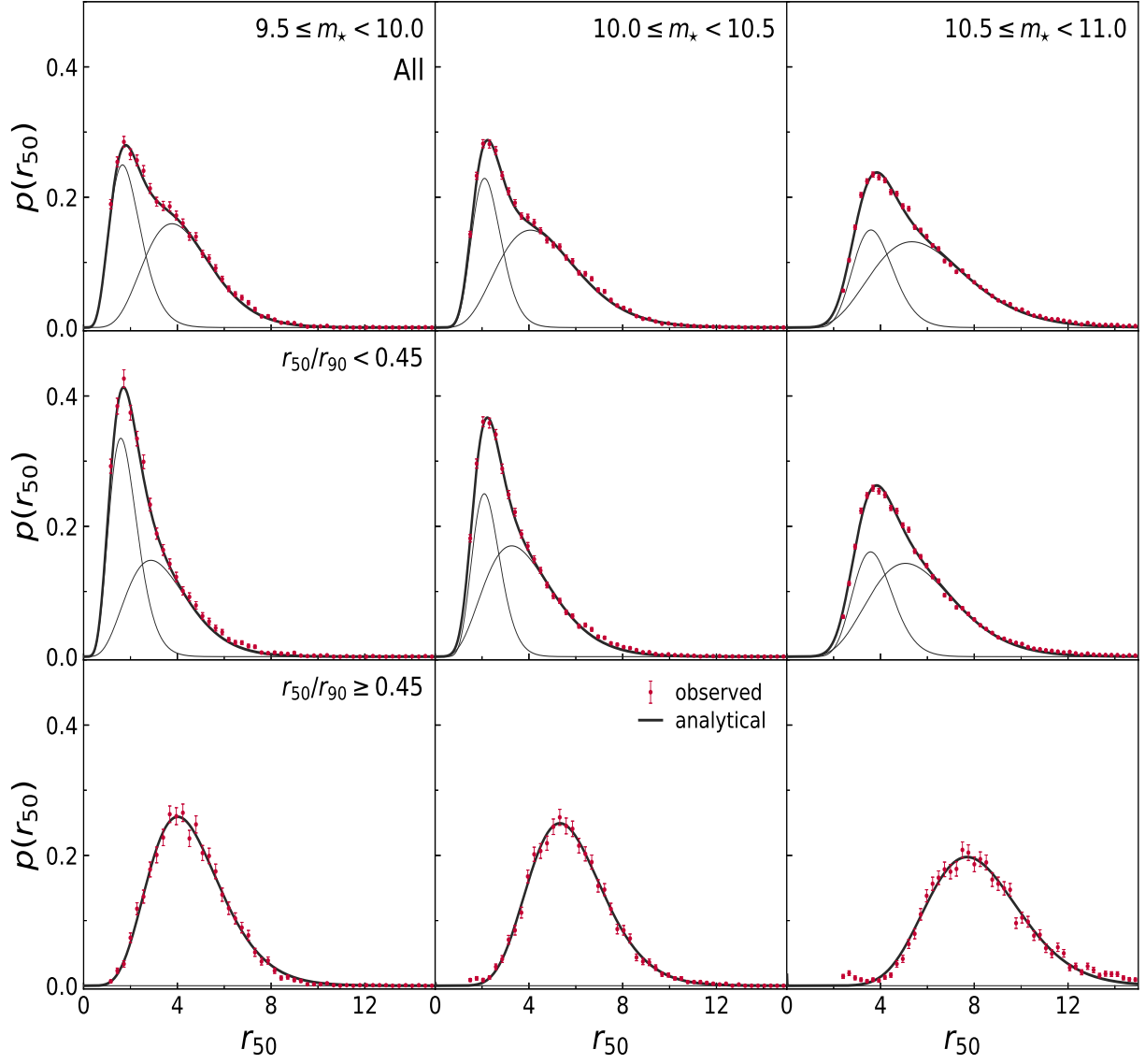


Fig. 2.— Probability density distributions of the half-light sizes of the selected local galaxies (red filled circles with Poisson errors) from the NASA-Sloan-Atlas catalog along with the best-fit Gamma mixture model (black thick solid lines) composed of two distinct modes (black thin solid lines) in three different stellar-mass ranges for three different cases of galaxy light concentrations, r_{50}/r_{90} .

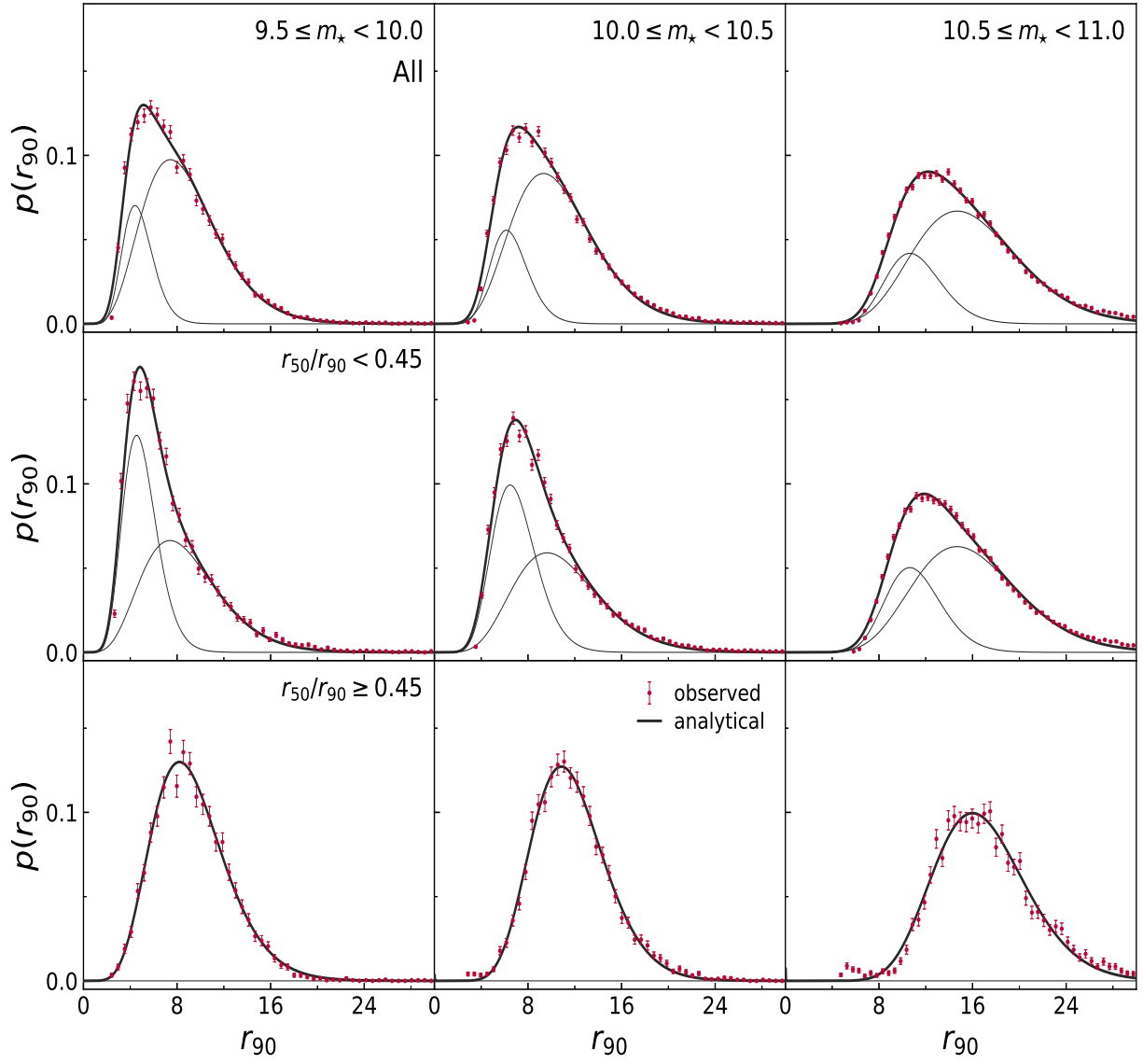


Fig. 3.— Same as Fig. 2 but of the 90%-light sizes.

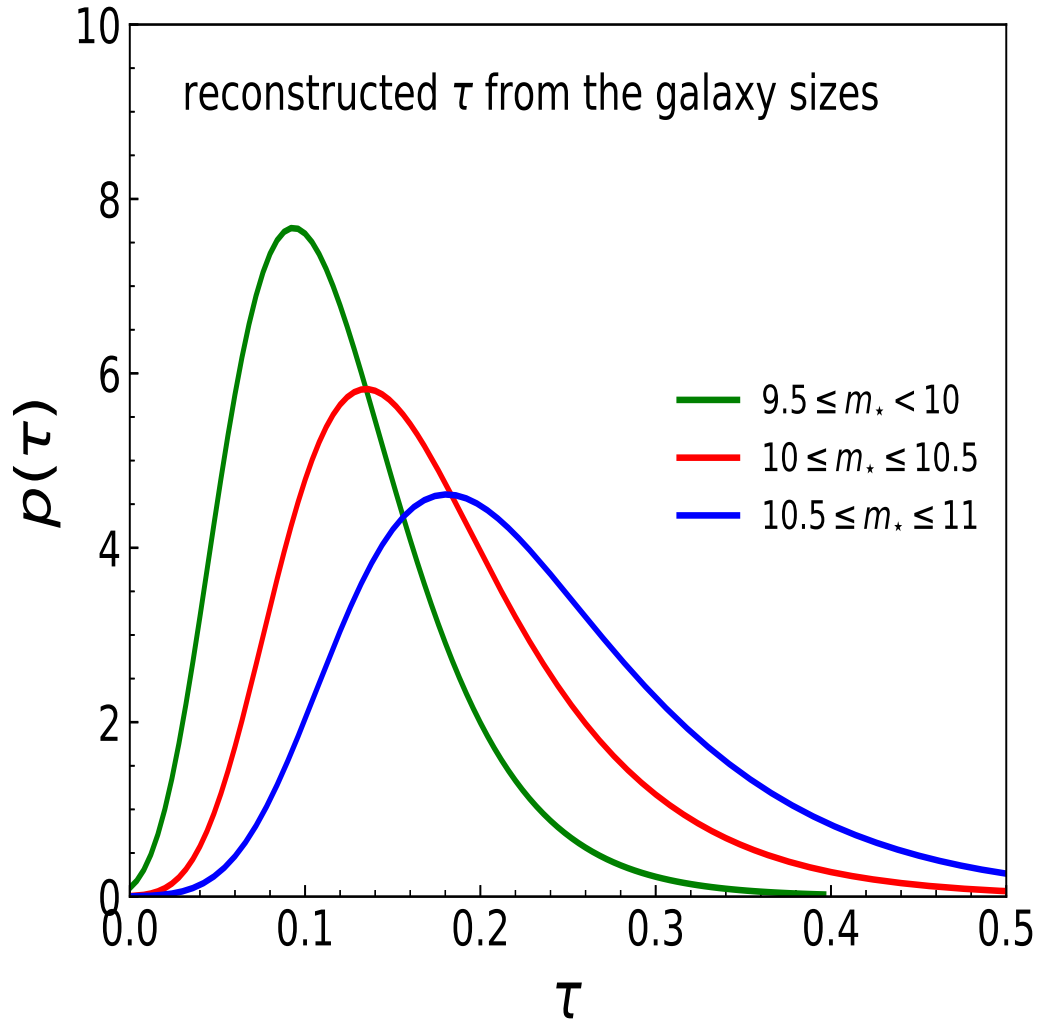


Fig. 4.— Reconstructed probability density distributions of the primordial spin factor from those of the observed galaxy optical sizes via Eq. (5) in three different m_* ranges. The reconstructed distributions match the real ones determined by numerical simulations directly from protogalactic inertia and initial tidal fields smoothed on three different scales.

Table 1. Numbers of the spiral galaxies and best-fit parameters of the analytical model for the size distributions in each mass range

M_{\star} [$h^{-1}M_{\odot}$]	N_s	k	10θ	$10^2\langle\alpha\rangle$	$10^2\sigma_{\alpha}$	r_{\min} [$h^{-1}\text{kpc}$]
[9.5, 10]	4824	7.98(8.31)	5.8(11.2)	2.5(1.25)	1.0(0.5)	1.02(2.13)
[10, 10.5]	5836	12.42(13.55)	4.7(8.6)	2.5(1.25)	1.8(1.5)	1.36(2.59)
[10.5, 11]	5719	16.36(17.76)	5.0(9.5)	2.5(1.25)	1.8(1.8)	2.28(4.5)